Mechanical and magnetic behavior of oligocrystalline Ni–Mn–Ga microwires

CrossMark

Peiqi Zheng [a], Nikole J. Kucza [b], Charles L. Patrick [b], Peter Müllner [b], David C. Dunand [a,*]

[a] Department of Materials Science & Engineering, Northwestern University, Evanston, IL 60208, USA
[b] Department of Materials Science & Engineering, Boise State University, Boise, ID 83725, USA

A B S T R A C T

Ni–Mn–Ga wires with sub-millimeter diameter, either as individual wires or as part of 2D or 3D wire assemblies, are promising candidates for actuators, sensors, magnetic cooling systems and energy harvesting devices. Here, we report on Ni–Mn–Ga wires with 200–400 μm diameter fabricated by the Taylor method, followed by annealing at 1050 °C for 1 h to achieve grain growth. The mechanical behavior of these oligocrystalline wires with bamboo grains was studied by tensile tests at room temperature. Wires with martensitic structure exhibited a very low Young's modulus of 5–8 GPa and superelastic behavior with twinning stresses of 22–30 MPa and maximum recoverable strain of 3.5%, and accumulated a plastic strain of ∼0.6% over 8 consecutive 0–50 MPa mechanical loading cycles. A 1 T rotating magnetic field caused the wire to bend to a curvature corresponding to a surface strain of 1.5%. During a full-field revolution, the wire deflected back and forth twice when the field direction was approximately perpendicular to the average wire direction. This effect was attributed to magnetic-torque-induced bending (MTIB) enabled by twinning.

1. Introduction

The magnetic shape memory effect (MSME), magneto-caloric effect (MCE) and damping capacities of Ni–Mn–Ga alloys near the stoichiometric Ni₂MnGa composition may provide the foundation for novel actuators, sensors, magnetic cooling systems and energy harvesting devices [1]. In particular, monocrystalline Ni–Mn–Ga are capable of magnetic-field-induced strain (MFIS) as high as 10% by twin-boundary motion [2]. However, the MFIS of polycrystalline Ni–Mn–Ga with fine grains and random textures is near zero because grain boundaries impede twin boundary movement or, equivalently, create strain incompatibilities between neighboring grains [3]. Recently, Dunand and Müllner [1] proposed that large MFIS in polycrystalline Ni–Mn–Ga could be enhanced by either growing the grains or shrinking the sample so that the grain size is comparable to a single crystal, thus allowing strain incompatibilities in grains to relax at their free surfaces. This concept was first demonstrated in foams with oligocrystalline struts consisting of large bamboo grains with twins spanning the full width of the struts (thus fulfilling the oligocrystalline definition of ratio of surface area to grain boundary area exceeding unity

[4–6]), where MFIS as high as 8.7% were measured [7,8]. Similarly, oligocrystalline Ni–Mn–Ga wires or ribbons with grain sizes similar to the wire diameter (bamboo structure) or the ribbon thickness were studied in a limited number of studies. Scheerbaum et al. [9] fabricated melt-spun Ni–Mn–Ga fibers with bamboo grain structure and achieved ∼1.0% MFIS measured from SEM image and confirmed by calculating strains in individual bamboo grains based on crystallographic orientation changes from a fiber (∼2.8 mm) at room temperature under a magnetic field up to 2 T.

From a technological standpoint, there is interest in miniaturization of MSMA-based devices using small MSMA particles such as: wires, ribbons, films, bilayers, multilayers, and pillars [10]. In particular, Ni–Mn–Ga microwires can be inserted within composites or constructed into 2D or 3D scaffolds by wire bonding [11]. In order to make Ni–Mn–Ga more suitable for isothermal high-frequency actuation and damping applications, Ni–Mn–Ga microwires with coarse grains could be embedded into a matrix directly as fibers or after being grounded into single crystal powders to develop smart composites [12,13].

Melt spinning [14–17] and the Taylor method [18–20] have been used to fabricate Ni–Mn–Ga wires or ribbons. A bamboo grain structure was achieved, with a melt spun wire, via annealing at 1100 °C for 2 h [9]. However, the surface of melt spun wires are very irregular (see Fig. 1 Ref. [9]), which may lead to early fracture due to stress concentration. The Taylor method as applied to

* Corresponding author.
   E-mail address: dunand@northwestern.edu (D.C. Dunand).

Ni–Mn–Ga microwire fabrication provides several advantages, which may be useful for bio-sensors: (i) wires are solidified within a glass sheath, which provides a smooth surface and could prevent corrosion as well as material evaporation, specifically Mn and Ga, during high temperature annealing [21]; (ii) it allows production of Ni–Mn–Ga wires as fine as ∼44 μm with a uniform circular cross-section [19].

With the exception of a very recent article [20] which is discussed later, no study has addressed the mechanical behavior and MFIS capability of Ni–Mn–Ga Taylor wires with coarse grains. Here, Taylor microwires with oligocrystalline bamboo grains are created and investigated in terms of composition, microstructure, phase constituents, along with mechanical and magnetic behavior.

2. Experimental procedures

2.1. Ni–Mn–Ga microwire preparation

Ni–Mn–Ga wires with 150–400 μm diameters and a length of up to 90 mm were manufactured using a custom-built Taylor machine. In the Taylor method [22,23] a metallic alloy and glass tube are drawn together in a single operation resulting in a glass-coated wire. Ni–Mn–Ga precursor rods with a nominal composition of $Ni_{50\pm0.5}Mn_{28.6\pm0.3}Ga_{21.4\pm0.2}$ at.% were prepared from Ni pellets (99.99 wt% purity, American Elements), Mn flakes (99.9 wt% purity, ESPI, cleaned with 1.3% nitric acid) and Ga shot (99.9999 wt% purity, Atlantic Metals) with an induction furnace. A Pyrex tube (Wilmad-LabGlass, softening point of 821 °C, ID of 8 mm and OD of 10 mm) was selected for its compatibility with Ni–Mn–Ga in terms of chemical properties, viscosity, and melting temperature. A fine long glass filament was drawn from the bottom of the tube using an oxy-acetylene torch and it was attached to an 82 mm diameter pulley for subsequent wire drawing. The alloy rod (∼8 mm in diameter, 2–3 mm in height, liquidus temperature of 1130 °C [24]) was placed inside the Pyrex tube. The system was first purged, then backfilled with argon (<1 atm was maintained), and finally melted by induction heating. Once melting was observed visually, the melt temperature was controlled to ± 10 °C by a single color pyrometer (Model: PSC-CS-Laser-2MH, Process Sensors) by adjusting the power of the induction heater. After the Pyrex tube was softened, by thermal conduction from the Ni–Mn–Ga melt, the pulley began rotating with a drawing speed of 26–103 μm/s. The distance between the induction coil and the pulley, the drawing speed, and the viscosities of the Pyrex tube and metallic melt all control the final diameter of the Ni–Mn–Ga Taylor wire. The limited hot zone of the induction coil paired with the constant drawing speed of the pulley creates a temperature discontinuity that caused the drawn glass-coated wire to break. A sand bed was used as cushioning and cooling media for the drawn wires. Upon cooling, the glass-coated Ni–Mn–Ga microwires and Ti getters were encapsulated in a quartz tube under low vacuum (∼50 Torr residual pressure) and subjected to heat treatments at 1050 °C for 1 h for grain growth and homogenization and 700 °C for 12 h for chemical ordering, followed by furnace cooling. The chemical ordering increases the MFIS by reducing structural and magnetic defects, which are known to impede the motion of twin boundaries [25]. The Pyrex cladding, which partially spalled off due to thermal shock upon rapid cooling after fabrication, was fully removed using 1600 grit sandpaper, instead of hydrofluoric acid which preferentially attacks Ga and alters the alloy composition of the Ni–Mn–Ga microwires. A SEM image of representative Ni–Mn–Ga Taylor microwire after removing the Pyrex glass coating is shown in Fig. 1.

Six Ni–Mn–Ga microwires were selected for further tests in this study. They are labeled S1 (diameter $d = 368 \pm 18$ μm, length $l = 14$ mm), S2 ($d = 210 \pm 10$ μm, $l = 12$ mm), S3 ($d = 210 \pm 12$ μm, $l = 12$ mm), S4 ($d = 280 \pm 12$ μm, $l = 20$ mm), S5 ($d = 249 \pm 13$ μm, $l = 13$ mm), and S6 ($d = 310 \pm 18$ μm, $l = 3.6$ mm). Tensile tests were conducted on wires S1, S2, S3 and S4. After mechanical and magneto-mechanical tests, short pieces (1–3 mm in length) were cut from selected wires for either composition characterization or metallographic preparation. Full-length samples of wires were tested in the Vibrating Sample Magnetometer (VSM) to determine the martensitic transformation temperature and Curie temperature. Additionally, X-ray diffraction (XRD) measurements were collected on the full length of the wires to determine phase composition.
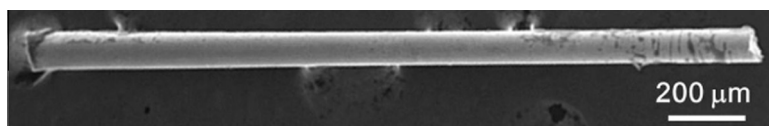
2.2. Composition, microstructure, phase and thermal properties

The composition of the Ni–Mn–Ga microwires was measured with a Hitachi-3400 scanning electron microscope (SEM) equipped with an energy-dispersive X-ray spectrometer (EDX). A standard sample, whose composition was determined via chemical analysis, was used for calibration purposes. The composition was determined by averaging measurements from three different cross-sections of each specimen. The SEM was operated at a 25 kV accelerating voltage and a 10 mm working distance for the analysis.

Short S1 and S3 pieces with 1–3 mm length were mounted into longitudinal and radial cross sections, and etched with Kalling's reagent #2 (5 g $CuCl_2$ + 100 ml HCl + 100 ml ethanol) following a final polishing with 0.06 μm colloidal silica.

The crystal structures of wires S1 and S2 were determined using Bruker AXS D8 Discover X-ray Diffractometer (XRD) with a Cu Kα source paired with an area detector. For phase analysis in the Bruker, the angles of the incident beam and of the detector center were simultaneously increased in increments of 5° so that the 2θ angle covered the range from 40° to 90°. The sample was placed on an acrylic sample holder and the sample stage was moved in X and Y such that the beam covered the entire sample while diffracted intensity was collected for 30 s. This procedure was repeated for different sample orientations varying by approximately 90°. While the structure of S5 was determined using a Rigaku Miniflex 600 with a Cu Kα source paired with a D/tex Ultra 1D Si detector. The measurements were collected in increments of 0.02° from 35° to 90°. The sample was centered inside an aluminum ring, supported by two-sided tape on top of polymer base, to allow sample rotation and ensure no stage interference during the scan. This procedure was repeated for different sample orientations varying by approximately 45° rotation along the short axis of the sample.

The thermodynamic equilibrium temperature of martensitic transformation (T_M) [26], taken as the mean of the martensite start temperature (M_s) and austenite finish temperature (A_f), and the Curie temperature (T_C) of the wires were determined using a MicroSense Model 10 Vibrating Sample Magnetometer (VSM). During VSM experiments, the wire was mounted perpendicular to the applied magnetic field and magnetization was measured as a function of temperature with a heating rate of 6 °C/min and a cooling rate of 4 °C/min.

2.3. Tensile tests

Wires S1–S4 were subjected to uniaxial tensile tests following the ASTM C1557 – 03(08) standard [27] at room temperature, using a TA Instruments RSA3 Dynamic Mechanical Analyzer (DMA). To avoid premature failure of the wires, i.e. damage in the gripping area or breaking during gripping due to the alloy brittleness, a mounting tab made of cardboard with a center hole of fixed gauge length (7.4 mm, 5.8 mm, 6.1 mm, 13 mm for wire S1, S2, S3, and S4 respectively) was used to support the wires while installing them into the tensile testing machine. Two rectangular G-10 epoxy/glass composite thin plates, ca. $5 \times 5 \times 1$ mm³ in dimensions (purchased from McMaster) were attached to the cardboard using double-sided tape. The two ends of the wires were fixed on the plates using cyanoacrylate glue. After the glue cured, the wire was embedded within the transparent glue and, therefore, remained undamaged when the whole frame was clamped into the tensile tester (see Fig. A1). After the specimen was mounted in the DMA, the cardboard frame was cut in two places, leaving the wire free to be tensile tested.

The uniaxial tensile force was applied by a microforce testing system and gave accurate stress measurement with a resolution of 0.9–3 kPa for wire diameters of 210–370 μm. The cross-head displacement was measured by a high resolution linear optical encoder with a strain resolution of 4–9×10^{-4}% for a gauge length of 5.8–13 mm. The TA Orchestrator software was used to control the system and collect the testing data. Before testing the Ni–Mn–Ga wire samples, bare copper wires (99.99% purity, Arcor) were used for calibration to determine the compliance of the load train, i.e. machine, superglue, tabs, which was used to correct the sample displacement. The strain-controlled tensile tests were carried out at room temperature at a constant strain rate of 1 μm/s. At the beginning of all cycles, a 2–5 MPa pretension was applied to straighten the wires.

2.4. Magneto-mechanical experiments

Rotating field experiments were performed with wires S5 and S6 in an optical magneto-mechanical device. A complete description of the device is given in Ref. [28]. In brief, a plastic tube was inserted in an electromagnet such that the tube axis lay parallel between the surfaces of the pole pieces, i.e. perpendicular to the

Fig. 1. SEM image of representative Ni–Mn–Ga microwire created by the Taylor method, with the diameter of ∼90 μm after removing Pyrex glass coating.
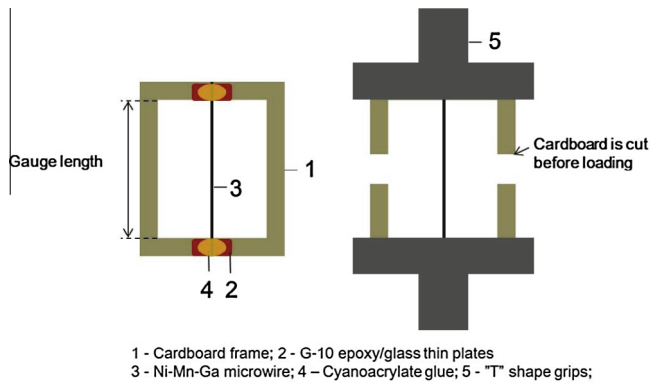
Fig. A1. Schematic of the cardboard frame technique for tensile testing of a single Ni–Mn–Ga microwire (not drawn to scale). A wire is adhesively bonded to a cardboard frame with a longitudinal slot. The cardboard with the bonded fiber, is clamped in the grips of the tensile testing machine. The cardboard frame is cut on both sides with scissors leaving the single microwire ready to be tested.

magnetic field direction. At one end of the tube, a Ni–Mn–Ga wire sample was mounted perpendicularly to the tube axis. The wire was glued at one of its ends to a sample holder, which was rigidly attached to the tube. On the other end, the wire was free. A camera and illumination assembly was rigidly mounted to the opposite end of the tube such that the wire was in the field of view of the camera. Tube and camera were attached to a gear and motor and were rotated with a stepper motor at 1° or 5° increments. Thus, while tube, sample and camera rotated counter-clockwise around the tube axis, the camera recorded a wire at rest in a clockwise rotating field. The field direction changed gradually from parallel to the wire axis (0°) to perpendicular to the wire axis (90°) back to parallel (180°) and again to perpendicular (270°) and finally to parallel (360°). In the following description, we discuss the experiment from the camera's coordinate system, which rotates with respect to the laboratory coordinate system.

A magnetic field of 1 T was applied parallel to the wire axis. The field was then rotated clockwise and 73 images were taken of the wire in 5° increments from 0° to 360°. For wire S5, the first rotating field experiments was performed at 21 ± 2 °C. The temperature was then raised first to 65 ± 2 °C (above A_f but below T_C) and then to 82 ± 2 °C (above T_C): at each temperature, a 360° rotating field experiment was performed.

3. Results and discussion

Wires S1 and S2 showed superelasticity and are discussed in details below. Wires S3 and S4 were linearly elastic up to stresses of 430 MPa at a strain of 0.8% (S3) and 560 MPa at a strain of 1.1% (S4) and are not discussed further, beyond acting as control experiments; their composition was shifted from the nominal value probably due to evaporative losses, so they displayed neither twinning nor stress-induced transformation. Wire S5 was used to demonstrate and analyze the magnetic field induced shape change, and wire S6 showed a similar behavior, demonstrating reproducibility (albeit at a larger diameter), and is not reported in detail here.

3.1. Structure and phase transformation temperatures of wires S1, S2, and S5

Fig. 2 shows low-field magnetization curves for wires S1, S2, and S5 recorded at a magnetic field of 0.025 T. The low-field magnetization curve of S1 (Fig. 2a) has a distinct plateau up to 70 °C, indicative of high magnetocrystalline anisotropy. Thus, we expect the wire to be martensitic at room temperature. The sudden drop of magnetization above 70 °C is due to the Curie temperature which is 83 ± 1 °C. We conclude that the martensite start temperature is at, or above, 110 °C, which is typical for non-modulated martensite [29,30].

The Curie temperature of wire S2 is 6 ± 3 °C, which is much lower than reported values for Ni–Mn–Ga Heusler alloys with typical Curie temperatures between 80 and 110 °C [29,30]. The low-field magnetization curve exhibits a maximum at −20 °C which indicates a structural phase transformation. Such a low
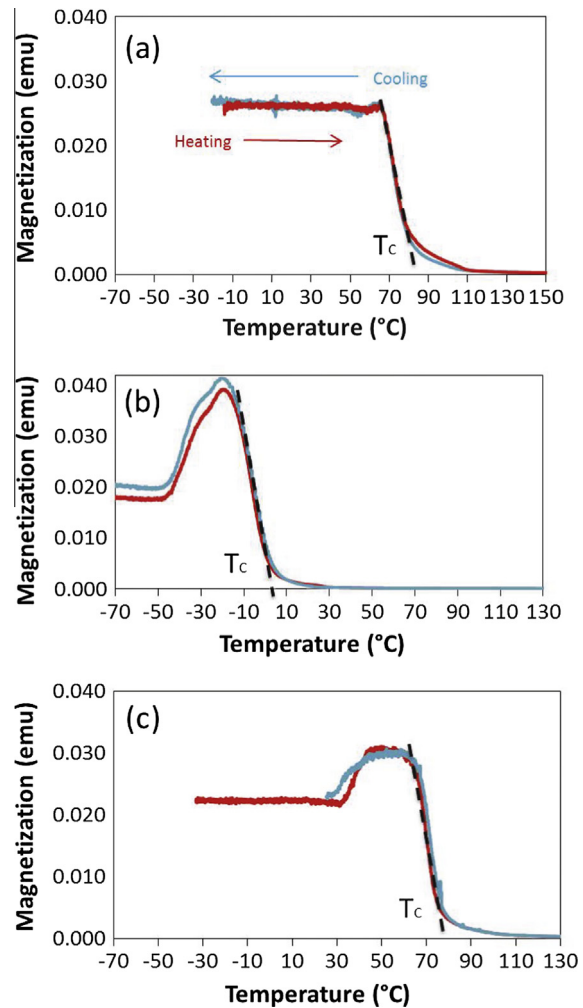
Fig. 2. Low-field magnetization curves for (a) S1, (b) S2, and (c) S5.

transformation temperature is atypical for a Heusler alloy with $e/a = 8.15$ [29]. However, the composition of this sample with 60 at.% Ni is outside the range of typical Heusler alloys and the phenomenological rule of thumb relating the e/a ratio to the martensite transformation temperature may not apply. A systematically study of magnetic properties as a function of excess Ni content concluded that ingots with 59.75 at.% Ni content or greater have phase segregation. Therefore, it was concluded that the low values of martensitic transformation and Curie temperature in wire S2 are due to the interaction of the second phase and the matrix alloy [26].

The low-field magnetization curve of wire S5 shows the characteristic features of a Ni–Mn–Ga Heusler alloy. The Curie temperature (T_C) is 77 ± 1 °C and a martensitic transformation (T_M) occurs at 43 ± 2 °C with: $M_s = 43 \pm 2$ °C, $M_f = 28 \pm 1$ °C, $A_s = 32 \pm 1$ °C, and $A_f = 43 \pm 2$ °C. The low-field magnetization of the martensite phase shows a plateau and is lower than that of the austenite phase.

Due to the small volume of the fibers and the small number of grains in each fiber, X-ray diffraction yielded only few reflections. For S1, two reflections were identified at $2\theta = 76.3°$ and $84.4°$. These peaks can be indexed as $(2 2 4)$ and $(2 4 2)$ for non-modulated martensite, consistent with the high M_s temperature. They may also be indexed for 14 M martensite, though. For S2, two reflections were identified at $2\theta = 44.5°$ and $2\theta = 64.7°$ which are consistent with the $(0 2 2)$ and $(0 0 4)$ austenite peaks. Although these X-ray results are not conclusive by themselves, our interpretation is consistent with the low-field magnetization curves shown in Fig. 2.
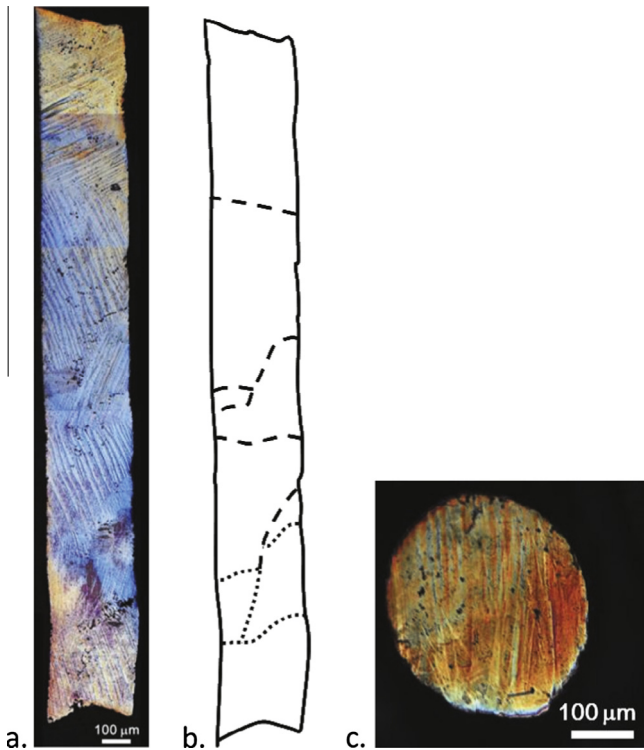
Fig. 3. (a) Polished and etched longitudinal cross-section of wire S1 showing multiple grains spanning across the whole wire. (b) Schematic of the wire with grain boundaries indicated by dashed (clearly visible grain boundary) and dotted (vaguely visible grain boundary) lines. (c) Lateral cross-section of the wire with a single grain covering the entire area.

3.2. Superelastic wires S1 and S2

3.2.1. Microstructure

Fig. 3a and c are representative cross sections of wire S1 along its longitudinal and radial directions. Fig. 3a shows that grains with single twin variants span across the whole wire cross section, illustrating that a bamboo grains structure was achieved after annealing the Taylor wire, whose as-solidified grain structure is fine due to its rapid cooling from the liquid phase. The bamboo grain structure is schematically shown in Fig. 3b and confirmed by the polished and etched radial cross-section of wire S1 in Fig. 3c, showing twin variants with one main orientation. The grain size is in the range of 100–400 µm, much larger than the ~10 µm grain size of the as-solidified wires. The fully martensitic structure observed in Fig. 3 indicates that the austenite/martensite transformation temperatures are above 150 °C, which is the upper boundary of VSM temperature measurement range. The S1 wire composition, $Ni_{54.1\pm0.3}Mn_{26.2\pm0.5}Ga_{19.7\pm0.3}$ at.% as listed in Table 1, shows the composition to be enriched in Ni (by ~4 at.%) and depleted in Mn and Ga (each by ~2 at.%) as compared to the precursor rods. X-ray scans revealed a tetragonal non-modulated (2 M) structure with lattice parameters $a = 0.549 \pm 0.001$ nm and $c = 0.651 \pm 0.001$ nm. The loss of Mn and Ga most probably occurred while the alloy was molten, as a result of the high vapor pressure of these elements.

3.2.2. Tensile properties

Fig. 4a shows a series of tensile stress–strain curves for wire S1, for eight load–unload loops where the maximum strain was increased from 0.7% to 3.5% at ambient temperature. The stress–strain curves exhibit the characteristic shape of superelastic materials, with a hysteresis loop on unloading where the strain is near fully recovered after each unloading. The superelastic recoverable strain for this wire increases from ~0.64% for the first loop with the lowest maximum stress of 34 MPa, to ~3.5% for the last loop with the highest maximum stress of 53 MPa. At the lowest stresses in each loop, a linear behavior is observed. Assuming that this represents elastic behavior without superelastic stress induced transformation, the slope of this early branch of the curves represents the Young's moduli. These are plotted as a function of maximum applied strain with loop number marked in Fig. 4b, and show a monotonically decreasing trend from 7.2 ± 0.1 GPa for the first loop to 5.0 ± 0.1 GPa for the last loop. The Young's modulus of Ni–Mn–Ga could change from 2 to 60 GPa due to the different original phase and phases formed by stress-induced phase transformations [31–33]. The Young's modulus of a single crystal Ni–Mn–Ga, 10 °C lower than its M_f, is 5 to 15 GPa [33]. The low Young's modulus of wire S1 is in agreement with its martensitic phase, as shown in Table 1. The modulus evolution from loop to loop may indicate the presence of stress-induced inter-martensitic transformations which were described in the high temperature Ni–Mn–Ga alloy [32,34] and mimic elastic recovery via transformation-induced recovery during unloading. The establishment of a preferred orientation of compliant grains during the load–unload loops may also result in the Young's modulus change. For stresses above ~35 MPa, the curves show an inflection, entering a second linear regime where stress increases more slowly with strain. This region is typical of superelasticity, where stress induced martensite occurs. Its onset, measured as a 0.1% offset yield strength during loading, $\sigma_{0.1}$, and plotted for all of the cycles in Fig. 4b, decreases from 36 to 23 MPa with increasing cycle number. For comparison, Ref. [20] reports values decreasing from 115 to ~100 MPa for wires with a much smaller diameter of 40 µm. A similar size effect was reported for compressive deformation of submicron Cu–Al–Ni micropillars [35]. The slope of the superelastic region decreases steadily with increasing cycle number, an effect reported as training in various shape-memory alloys and probably related to the selection of preferred martensitic variants that twin at lower stress than others [36–38].

On unloading, a first linear region correspond to elastic unloading of the martensite, with a slope corresponding to the Young's modulus, which is between 5.5 and 7.5 GPa, within error of the loading value. A superelastic region follows upon further unloading, at stresses lower than those on superelastic loading, indicating that the detwinning of the martensite upon loading is reversible. The stress hysteresis width in the superelastic range, $\Delta\sigma$, is shown as the difference between the upper plateau stress and the lower

Table 1
Composition, phase constituents, and transformation temperatures of wires S1, S2, S5 and S6 (A_s: austenite start temperature; A_f: austenite finish temperature; M_s: martensite start temperature; M_f: martensite finish temperature; T_c: Curie temperature).

Wire	Composition (at.%)			Transformation temperature by VSM (°C)					Crystal structure at room temperature
	Ni	Mn	Ga	A_s	A_f	M_s	M_f	T_c	
S1	54.1 ± 0.3	26.2 ± 0.5	19.7 ± 0.3	>150	>150	>150	>150	83 ± 1	Non-modulated martensite
S2	63.3 ± 5.9	17.9 ± 0.4	18.9 ± 0.6	<−30	<−30	<−30	<−30	6 ± 3	Cubic (austenite)
S5	53.3 ± 0.7	23.6 ± 0.6	23.1 ± 0.4	32 ± 1	43 ± 2	43 ± 2	28 ± 2	77 ± 1	Martensite
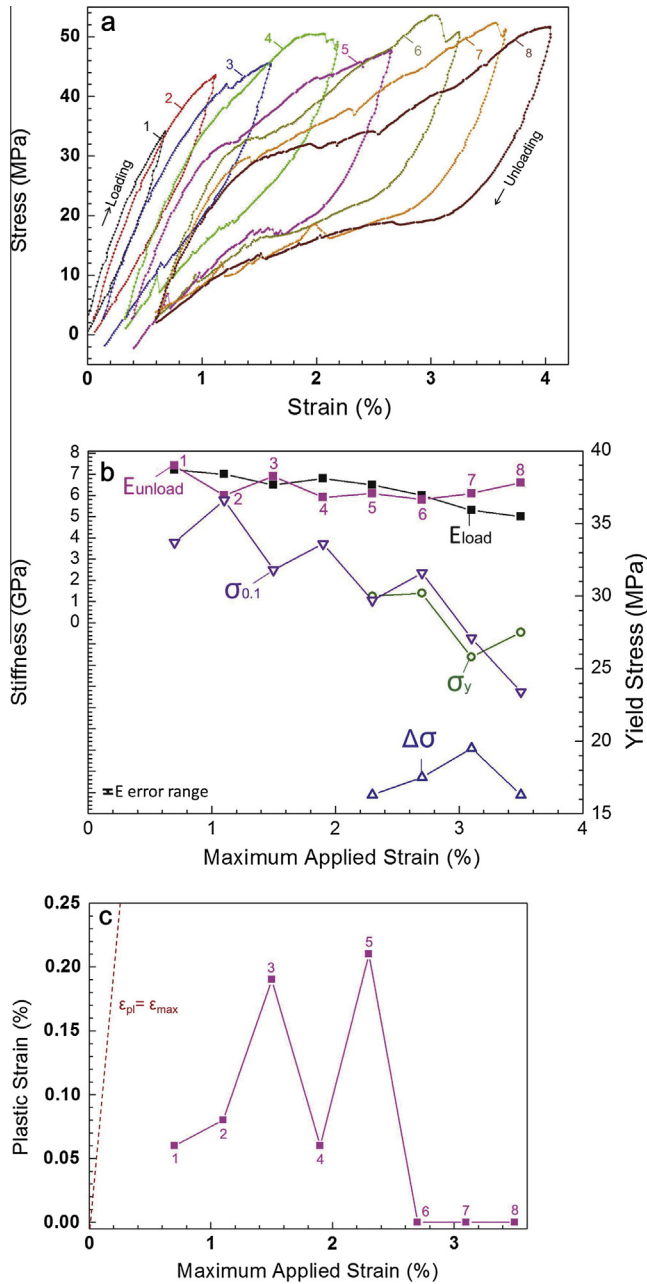
Fig. 4. (a) True stress–strain curves for wire S1 at room temperature. Curves with different colors correspond to consecutive cycles at increasing maximum applied strain; (b) Young's modulus during loading and unloading (marked as E_{load} and E_{unload}) and yield stresses (labeled σ_y, $\sigma_{0.1}$, and $\Delta\sigma$) for each cycle in (a); (c) plastic strain (ε_{pl}) as a function of the maximum strain (ε_{max}) applied for each cycle in curve (a). The cycle numbers are marked. Error bars for stress and strain are smaller than the symbol size. (For interpretation of the references to color in this figure legend, the reader is referred to the web version of this article.)

Fig. 5. (a) True stress–strain curves for wire S2 at room temperature. Curves with different colors correspond to consecutive cycles at increasing maximum applied strain; (b) Young's modulus during loading and unloading (marked as E_{load} and E_{unload}) and yield stresses (labeled σ_y and $\Delta\sigma$) for each cycle in (a); (c) plastic strain (ε_{pl}) as a function of the maximum strain (ε_{max}) applied for each cycle in curve (a). The cycle numbers are marked. Error bars for stress and strain are smaller than the symbol size. (For interpretation of the references to color in this figure legend, the reader is referred to the web version of this article.)

plateau stress in Fig. 4b and remains relatively constant at 18 ± 2 MPa. Finally, Fig. 4c shows, as a function of the maximum strain for each cycle, the residual plastic strain at the end of each cycle. This unrecoverable strain is small in the first five loops, and then zero within experimental measurement in the last three. The dashed line denotes the condition where ε_{pl} equals ε_{max}, that is when the strain recovery rate is 0%. It is apparent that shape recovery is high, between 87.3% for cycle 3 and 100% for cycles 6–8. After cycle 8, wire S1 fractured while uninstalling from the instrument.

Superelastic behavior was also observed in wire S2. Its tensile stress–strain curves are shown in Fig. 5a. The maximum strain was increased from 0.4% to 2.0% at ambient temperature over 8 load–unload loops. The superelastic recoverable strain for this wire increases from ~0.2% for the first loop with the lowest maximum stress of 27 MPa, to ~1.88% for the last loop with the maximum stress of 44 MPa. At the end of unloading at very low applied stress, a small stress peak was repeatedly observed for all cycles (except cycles 1 and 2 with low maximum strain) indicating that the wire undergoes contraction more rapidly than the instrument is reducing strain. The peaks and steps in Figs. 4a and 5a may be explained by the occurrence of intermartensitic transformations [39] on

unloading. The Young's moduli are plotted as a function of maximum applied strain in Fig. 5b. During loading, the Young's modulus is stable in the first five loops (∼6 GPa, very close to the value of 6.4 GPa reported in Ref. [20]) and increases to as high as ∼8 GPa for cycle 7. The twinning stress, σ_y, i.e. the critical stress required to reorient twin variants, decreases from 27 to 23 MPa with increasing cycle number, as shown in Fig. 5b, illustrating mechanical training in wire S2 [40]. The difference in behavior between wires S1 and S2 is most likely due to their different compositions and transformation temperatures.

The Young's modulus during unloading ranges between 5.5 and 7.8 GPa. The stress hysteresis width in the superelastic range, $\Delta\sigma$, is shown in Fig. 5b and it also remains constant at 17.5 ± 1 MPa. Finally, Fig. 5c shows, as a function of the maximum strain for each cycle, the residual plastic strain at the end of each cycle. The shape recovery is high, between 93% for cycle 3 and 78% for cycle 7. Wire S2 fractured at the 9th loop at a strain of ∼1.1% under a stress of 25 MPa.

Chernenko et al. [41] conducted tensile tests using $\langle 0\,0\,1\rangle_A$ -oriented high temperature Ni–Mn–Ga single crystals with martensitic transformation temperatures of ∼312 °C and obtained multistep superelastic strain of about 9% at ∼320 °C. The corresponding Young's modulus was ∼15 GPa and the highest stress ∼180 MPa. Recently, this research group estimated martensitic and intermartensitic transformations from the standpoint of elastic modulus dependence on temperature. The quasi-equilibrium stress–temperature phase diagrams of the $L2_1$–5M, 5M–7M and 7M–2M phase transitions were also compared with thermodynamic estimations and ab initio calculations and found to be in agreement [42]. Similarly, the large superelasticity of wire S1 and S2 may be attributed to stress-induced martensitic twin variants reorientation and/or intermartensitic transformations during loading and unloading. This leads to large strains without fracture due to the oligocrystalline structure which reduces incompatibility strains between neighboring grains in the wires. In-situ X-ray diffraction during tensile tests could be carried out for phase evolution exploration but is outside the scope of this paper. We finally note that oligocrystalline copper-based superelastic alloys have strong size effects as well [4–6,18,35], but that thermal effects associated with the thermal phase transformation further complicate the size effect.

3.3. Rotating field experiments on wire S5

For the rotating field experiment performed at room temperature in 5° increments, starting at a field angle of 0°, which is pointing to the right in Fig. 6a, the wire S5 was almost straight. Upon field rotation (clockwise), the wire slowly bent into the field direction, i.e. its free end tipped downwards. At an angle of 110°, the wire suddenly deflected to the opposite direction, i.e. with its free end pointing upwards. The wire then slowly bent again in the field direction until the field angle reached 290° when the wire deflected again abruptly to the opposite, upwards direction. Upon further field rotation up to 360° the wire continued bending slowly in the downwards field direction. Thus, the bending response repeated twice during one revolution of the magnetic field.

The deflection of the wire was evaluated at a constant position 3 mm away from the fixture (indicated with vertical lines in Fig. 6). The maximum deflection, calculated from the highest and lowest positions achieved by the wire, was significantly reduced when the experiments were performed at higher temperature. At 65 °C and 82 °C, the maximum deflections were 0.083 mm and 0.017 mm, as compared to 1.846 mm at 21 °C (Fig. 6) where the wire was martensitic. The magnetic field exerted a torque $\Theta = \mu_0 MHV\sin\varphi$ on the wire where M and H are saturation magnetization and magnetic field magnitude, V is the volume of the wire, and φ is the field direction measured clockwise in Fig. 6 with zero pointing
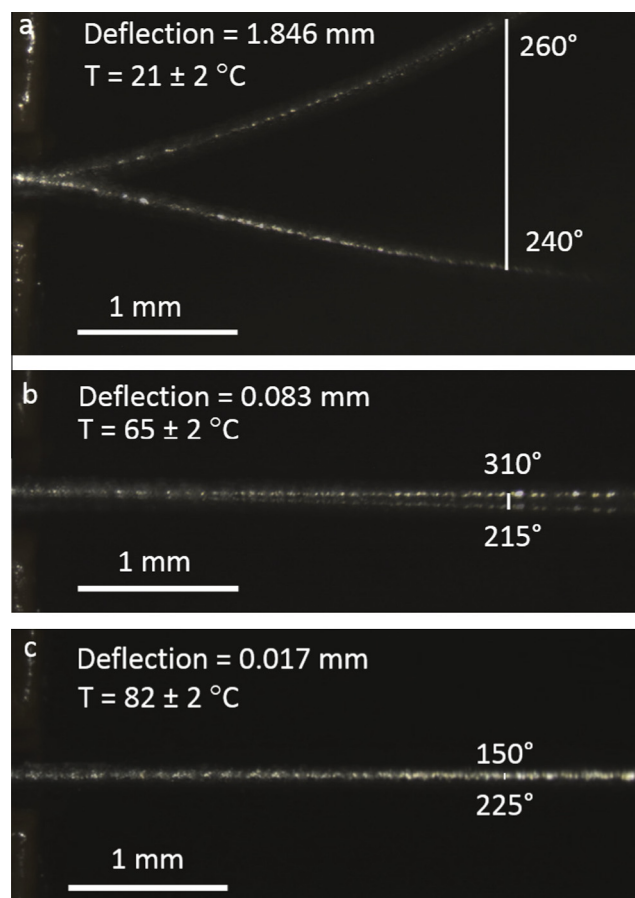
Fig. 6. Bending of Ni–Mn–Ga wire S5 in a magnetic field. Each image contains two superposed pictures showing the wire at maximum deflection. (a) At room temperature where the wire was in its ferromagnetic martensite phase, the wire bent strongly in the magnetic field and switched abruptly from pointing downwards to pointing upwards when the magnetic field was incremented from 110° to 115°. (b) At 65 °C, the wire was in its austenite phase yet below the Curie temperature. The wire bent elastically. (c) At 82 °C, the wire was paramagnetic and bent only very slightly in the magnetic field. The vertical lines in (a) and (b) indicate where the deflection was evaluated.

horizontally to the left. In this geometry and using M = 50 emu/g and μ_0H = 1 T, the maximum torque is about 10 m Nm. The wire switched position abruptly when the magnetic field was approximately perpendicular to the average wire direction, i.e. when the torque approached the maximum value. For a round bar with diameter d loaded under bending, the maximum axial normal stress is $\sigma_{max} = 32\Theta/\pi d^3$, which exceeds 100 MPa in the present situation. This stress is much larger than the twinning stress and is expected to causes the wire to bend plastically by twinning. Wire bending causes an axial surface strain $\varepsilon = d/2R$, where R is the radius of curvature. The maximum deflection of 2.2 mm corresponds to a radius of curvature of 8 mm, leading to a strain at the outer wire surface of ∼1.5%.

At 65 °C, the wire was austenitic and just below its Curie temperature, where the saturation magnetization is much reduced. The resulting local stresses were not sufficient to cause stress-induced martensite and the wire thus bent elastically. A deflection of 0.09 mm corresponds to a strain of ∼0.1% at the wire surface which is expected to be accommodated elastically. At the higher temperature, 82 °C, the austenitic wire was paramagnetic. The magnetic-field-induced torque was thus negligible and, as expected, almost no bending occurred.

Fig. 7 shows the axial surface strain of wire S5 where the magnetic field was cycled between 65° and 120° in 1° increments.
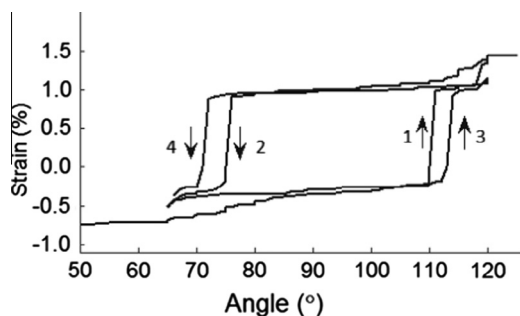
Fig. 7. Axial normal strain at the surface of the wire S5 due to bending in the magnetic field. When the magnetic field reached an angle of 110°, the wire deflected causing a reversal of the strain (Point 1). Above 120°, curvature and strain remained constant. Upon reduction of the field angle, the curvature remained nearly constant down to a field angle of 75° where the wire deflected back abruptly (Point 2). Upon repetition of the field path, the wire deflected back and forth again (Points 3 and 4) with a slightly larger hysteresis.

Upon increasing the magnetic field angle from 50°, the surface strain slowly increased. When the field angle reached 110° (Point 1), the wire deflected to the opposite side and the strain reversed sign. Above 120°, curvature and strain remained almost constant. The field angle was then lowered and the surface strain reduced slowly until the field direction reached 75° where the wire deflected back (Point 2). Upon repetition of the field path, the wire deflected back and forth again (Points 3 and 4) with a slightly larger hysteresis. Whether this increase is a statistical variation or a systematic trend due to accumulation of defects remains to be studied.

4. Conclusions

Ni–Mn–Ga microwires were solidified within a Pyrex tube drawn together using the Taylor technique. An oligocrystalline grain structure and L2$_1$ crystal structure in the austenite phase were obtained in these microwires by subsequent homogenizing at 1050 °C for 1 h and aging at 700 °C for 12 h, with varying crystal structures (austenite and martensite) at room temperature, depending on composition. Tensile superelastic deformation up to ∼3.5% in the martensite phase and linear elastic deformation of up to 1.3% in the austenite phase at ambient temperature, both recoverable upon unloading, were observed by uniaxial tensile tests on wires of various compositions. Magnetic-torque-induced bending (MTIB) caused large recoverable bending deflections accommodated by twinning in a Ni–Mn–Ga microwire in the martensite phase.

References

[1] D.C. Dunand, P. Müllner, Size effects on magnetic actuation in Ni–Mn–Ga shape-memory alloys, Adv. Mater. 23 (2011) 216–232.
[2] A. Sozinov, A.A. Likhachev, N. Lanska, K. Ullakko, Giant magnetic-field-induced strain in NiMnGa seven-layered martensitic phase, Appl. Phys. Lett. 80 (2002) 1746–1748.
[3] P. Lazpita, G. Rojo, J. Gutierrez, J.M. Barandiaran, R.C. O'Handley, Correlation between magnetization and deformation in a NiMnGa shape memory alloy polycrystalline ribbon, Sens. Lett. 5 (2007) 65–68.
[4] S. Ueland, Y. Chen, C.A. Schuh, Oligocrystalline shape memory alloys, Adv. Funct. Mater. 22 (2012) 2094–2099.
[5] S. Ueland, C. Schuh, Superelasticity and fatigue in oligocrystalline shape memory alloy microwires, Acta Mater. 60 (2012) 282–292.
[6] A. Lai, Z. Du, C. Gan, S. CA, Shape memory and superelastic ceramics at small scales, Science 341 (2013) 1505–1508.
[7] Y. Boonyongmaneerat, M. Chmielus, D.C. Dunand, P. Müllner, Increasing magnetoplasticity in polycrystalline Ni–Mn–Ga by reducing internal constraints through porosity, Phys. Rev. Lett. 99 (2007) 247201.
[8] M. Chmielus, X.X. Zhang, C. Witherspoon, D.C. Dunand, P. Müllner, Giant magnetic-field-induced strains in polycrystalline Ni–Mn–Ga foams, Nat. Mater. 8 (2009) 863–866.
[9] N. Scheerbaum, O. Heczko, J. Liu, D. Hinz, L. Schultz, O. Gutfleisch, Magnetic field-induced twin boundary motion in polycrystalline Ni–Mn–Ga fibres, New J. Phys. 10 (2008) 073002.
[10] R. Varga, T. Ryba, Z. Vargova, K. Saksl, V. Zhukova, A. Zhukov, Magnetic and structural properties of Ni–Mn–Ga Heusler-type microwires, Scripta Mater. 65 (2011) 703–706.
[11] S. Glock, X.X. Zhang, N.J. Kucza, P. Müllner, V. Michaud, Structural, physical and damping properties of melt-spun Ni–Mn–Ga wire–epoxy composites, Composites 63 (2014) 68–75.
[12] N. Scheerbaum, D. Hinz, O. Gutfleisch, K.H. Müllner, L. Schultz, Textured polymer bonded composites with Ni–Mn–Ga magnetic shape memory particles, Acta Mater. 55 (2007) 2707–2713.
[13] M. Lahelin, Studies on Polymeric Composites with Ni–Mn–Ga Alloys and Carbon Nanotubes, Aalto University, 2011.
[14] A.K. Panda, M. Ghosh, A. Kumar, A. Mitra, Magnetic transitions and structure of a NiMnGa ferromagnetic shape memory alloy prepared by melt spinning technique, J. Magn. Magn. Mater. 320 (2008) 116–120.
[15] J. Liu, T.G. Woodcock, N. Scheerbaum, O. Gutfleisch, Influence of annealing on magnetic field-induced structural transformation and magnetocaloric effect in Ni–Mn–In–Co ribbons, Acta Mater. 57 (2009) 4911–4920.
[16] J.L.S. Llamazares, B. Hernando, C. Garcia, J. Gonzalez, L.L. Escoda, J.J. Sunol, Martensitic transformation in Ni50.4Mn34.9In14.7 melt spun ribbons, J. Phys. D Appl. Phys. 42 (2009) 045002.
[17] P. Ochin, A. Dezellus, P. Plaindoux, J. Pons, P. Vermaut, R. Portier, E. Cesari, Shape memory thin round wires produced by the in rotating water melt-spinning technique, Acta Mater. 54 (2006) 1877–1885.
[18] Y. Chen, X.X. Zhang, D.C. Dunand, C.A. Schuh, Shape memory and superelasticity in polycrystalline Cu–Al–Ni microwires, Appl. Phys. Lett. 95 (2009) 171906.
[19] R. Varga, T. Ryba, K. Saksl, V. Zhukova, J. Gonzalez, A. Zhukov, Studies of magnetic and structural properties of Ni–Mn–Ga Heusler-type microwires, J. Optoelectron. Adv. M 14 (2012) 257–261.
[20] Y. Zhang, M. Li, Y.D. Wang, J.P. Lin, K.A. Dahmen, Z.L. Wang, P.K. Liaw, Superelasticity and serration behavior in small-sized NiMnGa alloys, Adv. Eng. Mater. 16 (2014) 955–960.
[21] G.R.M.M.J. Spottorno, Magnetic Sensors for Biomedical Applications, in: K. Kuang (Ed.), Magnetic Sensors – Principles and Applications, TnTech, 2012, pp. 125–150.
[22] I.W. Donald, Production, properties and applications of microwire and related products, J. Mater. Sci. 22 (1987) 2661–2679.
[23] I.W. Donald, B.L. Metcalfe, The preparation, properties and applications of some glass-coated metal filaments prepared by the Taylor-wire process, J. Mater. Sci. 31 (1996) 1139–1149.
[24] D.L. Schlagel, Y.L. Wu, W. Zhang, T.A. Lograsso, Chemical segregation during bulk single crystal preparation of Ni–Mn–Ga ferromagnetic shape memory alloys, J. Alloys Comp. 312 (2000) 77–85.
[25] M.L. Richard, J. Feuchtwanger, S.M. Allen, R.C. O'Handley, P. Lazpita, J.M. Barandiaran, J. Gutierrez, B. Ouladdiaf, C. Mondelli, T. Lograsso, D. Schlagel, Chemical order in off-stoichiometric Ni–Mn–Ga ferromagnetic shape-memory alloys studied with neutron diffraction, Philos. Mag. 87 (2007) 3437–3447.
[26] V.V. Khovaylo, V.D. Buchelnikov, R. Kainuma, V.V. Koledov, M. Ohtsuka, V.G. Shavrov, T. Takagi, S.V. Taskaev, A.N. Vasiliev, Phase transition in Ni2 + xMn1 − xGa with a high Ni excess, Phys. Rev. B 72 (2005) 1–10.
[27] ASTM Standard C1557, Standard Test Method for Tensile Strength and Young's Modulus of Fibers, ASTM International, West Conshohocken, PA, 2003.
[28] A. Rothenbühler, E.H.B. Smith, P. Müllner, Application of image processing to track twin boundary motion in magnetic shape memory alloys, SPIE (2012).
[29] V.A. Chernenko, Compositional instability of beta-phase in Ni–Mn–Ga alloys, Scripta Mater. 40 (1999) 523–527.
[30] N. Lanska, O. Söderberg, A. Sozinov, Y. Ge, K. Ullakko, V.K. Lindroos, Composition and temperature dependence of the crystal structure of Ni–Mn–Ga alloys, J. Appl. Phys. 95 (2004) 8074–8078.
[31] V.A. Chernenko, J. Pons, C. Segui, E. Cesari, Premartensitic phenomena and other phase transformations in Ni–Mn–Ga alloys studied by dynamical mechanical analysis and electron diffraction, Acta Mater. 50 (2002) 53–60.
[32] V.A. Chernenko, C. Segui, E. Cesari, J. Pons, V.V. Kokorin, Sequence of martensitic transformations in Ni–Mn–Ga alloys, Phys. Rev. B 57 (1998) 2659–2662.
[33] Z.M. Peng, X.J. Jin, Y.Z. Fan, T.Y. Hsu, S.M. Allen, R.C. O'Handley, Internal friction and modulus changes associated with martensitic and reverse transformations in a single crystal Ni48.5Mn31.4Ga20.1 alloy, J. Appl. Phys. 95 (2004) 6960–6962.

[34] U. Gaitzsch, M. Pötschke, S. Roth, N. Mattern, B. Rellinghaus, L. Schultz, Structure formation in martensitic $Ni_{50}Mn_{30}Ga_{20}$ MSM alloy, J. Alloys Comp. 443 (2007) 99–104.

[35] J. San Juan, M. No, C. Schuh, Thermomechanical behavior at the nanoscale and size effects in shape memory alloys, J. Mater. Res. 26 (2011) 2461–2469.

[36] L. Straka, O. Heczko, H. Hänninen, Activation of magnetic shape memory effect in Ni–Mn–Ga alloys by mechanical and magnetic treatment, Acta Mater. 56 (2008) 5492–5499.

[37] U. Gaitzsch, H. Klauß, S. Roth, L. Schultz, Magnetomechanical training of single crystalline Ni–Mn–Ga alloy, J. Magn. Magn. Mater. 324 (2012) 430–433.

[38] U. Gaitzsch, M. Pötschke, S. Roth, B. Rellinghaus, L. Schultz, Mechanical training of polycrystalline 7M $Ni_{50}Mn_{30}Ga_{20}$ magnetic shape memory alloy, Scripta Mater. 57 (2007) 493–495.

[39] V.A. Chernenko, J. Pons, E. Cesari, K. Ishikawa, Stress–temperature phase diagram of a ferromagnetic Ni–Mn–Ga shape memory alloy, Acta Mater. 53 (2005) 5071–5077.

[40] K. Otsuka, C.M. Wayman, Superelasticity effects and stress-induced martensitic transformations in Cu–Al–Ni alloys, Acta Mater. 24 (1976) 207–226.

[41] V.A. Chernenko, E. Villa, S. Besseghini, J.M. Barandiaran, Giant two-way shape memory effect in high-temperature Ni–Mn–Ga single crystal, Phys. Proc. 10 (2010) 94–98.

[42] V.A. Chernenko, E.V.J.M. Barandiaran, T. Kakeshita, T. Fukuda, T. Terai, S. Besseghini, Peculiarities of superelastic tensile behavior of Ni–Mn–Ga and Ni(Co)–Fe–Ga single crystals, in: Shape Memory & Superelastic Technology Conference and Exposition, Prague, Czech Republic, 2013.